



Evaluation of a novel 8-channel RX coil for speech production MRI at 0.55 T

Felix Muñoz¹ · Yongwan Lim² · Sophia X. Cui³ · Helmut Stark⁴ · Krishna S. Nayak^{1,2}

Received: 19 February 2022 / Revised: 25 July 2022 / Accepted: 8 August 2022

© The Author(s), under exclusive licence to European Society for Magnetic Resonance in Medicine and Biology (ESMRMB) 2022

Abstract

Objective Speech production MRI benefits from lower magnetic fields due to reduced off-resonance effects at air-tissue interfaces and from the use of dedicated receiver coils due to higher SNR and parallel imaging capability. Here we present a custom designed upper airway coil for ¹H imaging at 0.55 Tesla and evaluate its performance in comparison with a vendor-provided prototype 16-channel head/neck coil.

Materials and methods Four adult volunteers were scanned with both custom speech and prototype head–neck coils. We evaluated SNR gains of each of the coils over eleven upper airway volumes-of-interest measured relative to the integrated body coil. We evaluated parallel imaging performance of both coils by computing g-factors for SENSE reconstruction of uniform and variable density Cartesian sampling schemes with $R=2, 3$, and 4.

Results The dedicated coil shows approximately 3.5-fold SNR efficiency compared to the head–neck coil. For $R=2$ and 3, both uniform and variable density samplings have g-factor values below 1.1 in the upper airway region. For $R=4$, g-factor values are higher for both trajectories.

Discussion The dedicated coil configuration allows for a significant SNR gain over the head–neck coil in the articulators. This, along with favorable g values, makes the coil useful in speech production MRI.

Keywords Speech production MRI · 0.55 Tesla · Low-field MRI · Receiver coil

Introduction

Speech production involves the complex coordination of different vocal organs in the upper and lower respiratory airways. There are numerous benefits to the study of speech production dynamics. These include aiding in understanding what articulatory mechanism explain the inter and intrasubject variability of speech as well as in understanding language disorders [1], aiding in clinical assessment of various diseases, such as tongue cancer, clefts of the lips, and vocal

cord polyps [2–4]. Another benefit includes capturing articulatory motion for use in articulation-to-speech synthesis to help patients regain their ability to communicate after a laryngectomy [5].

There are different modalities used to study speech production, including real-time MRI (RT-MRI), electromagnetic articulography [6], ultrasound [7], and X-ray video fluoroscopy [8, 9]. In comparison to these modalities, RT-MRI provides several advantages in terms of (a) lack of ionizing radiation as opposed to X-ray fluoroscopy, (b) the ability to image arbitrary planes as opposed to ultrasound, and (c) the ability to visualize deep structures (e.g., velum, epiglottis) which is not possible with ultrasound or electromagnetic articulography. The performance of speech production RT-MRI at conventional field strengths (1.5 T and 3 T) is limited by susceptibility artifacts at the air-tissue interfaces [10]. These artifacts often appear as spatial blur, and are both dynamic and precisely at the features of interest, the articulator boundaries [11, 12]. RT-MRI at lower field strengths, such as 0.55 T, will have lower susceptibility-related

✉ Felix Muñoz
jdfelix@usc.edu

¹ Department of Biomedical Engineering, University of Southern California, Los Angeles, CA, USA

² Ming Hsieh Department of Electrical and Computer Engineering, University of Southern California, Los Angeles, CA, USA

³ Siemens Medical Solutions USA, Inc., Los Angeles, CA, USA

⁴ Stark Contrast, Erlangen, Germany

off-resonance, and the potential for improved performance [13, 14].

The use of dedicated upper airway coils provides a boost in SNR over standard head coils, because they experience higher loading from the region of interest as the coils can be placed closer to the articulators. They also experience lower noise and better parallel imaging performance due to highly localized elements with diverse coil sensitivity over the region of interest. This is particularly important at low field because SNR is lower than at higher field strengths. Dedicated coils also allow for imaging with targeted field-of-view (FOV), which reduces the minimum amount of encoding needed to make images. Improved SNR is extremely valuable for high-resolution structural imaging [15, 16]. Improved SNR and the reduced FOV is extremely valuable for dynamic and real-time imaging [17]. MRI systems operating at lower field strengths (e.g., 0.55 T) with high-performance gradients have numerous advantages for dynamic and real-time imaging [17, 18], which is our primary motivation. We provide an example of fast dynamic imaging of human speech production using the dedicated upper airway coil presented in this work in Online Resource 1.

The gain in SNR with these dedicated coils has been investigated at various field strengths. At 1.5 T, an 8-channel upper airway coil was observed to yield an SNR gain of 3–5 over a standard head and neck coil in the articulators [19]. At 3 T, a 16-channel upper airway coil provided an eightfold gain in SNR over an 8-channel head and neck coil in the articulators [18]. In this work, we present a custom designed upper airway (UA) coil for ^1H imaging at 0.55 Tesla (23.6 MHz) and evaluate its performance in comparison with a vendor-provided prototype head/neck (HN) coil over 11 upper airway volumes-of-interest (VOIs). We also evaluate the parallel imaging performance of both coils using Cartesian SENSE with uniform and variable density undersampling.

Materials and methods

Upper airway coil design

Two separate coil phased arrays were constructed with four copper elements each. For each of the two arrays, a polyvinyl chloride (PVC) cover was heated and shaped to conform to the anatomy of the jaw, and the elements were attached to the cover. Electronics for matching, decoupling, and detuning were then incorporated. This setup along with a schematic is illustrated in Fig. 1. Finally, a flexible holder was set up to fix the assembly to different patient shapes.

The elements are made out of thick (200 μm) copper bands to minimize coil losses. Each element contains both active and passive detuning circuits to detune the coils

during RF transmission. As an added safety feature during RF transmission, an RF fuse is added to each element. In each array, the four elements overlap in such a way as to minimize the coupling of the neighboring elements. This process is referred to as geometric decoupling. To decouple diagonal elements, a common capacitor is used to cancel out the reactance of the mutual inductance. This process is referred to as capacitive decoupling [20]. Additionally, pre-amplifier decoupling was used to decouple non-neighboring elements. Geometric and capacitive decoupling were determined iteratively while loaded with a subject until desired decoupling coefficients were achieved. Q-factors were determined using a network analyzer, with both loaded and unloaded conditions. The typical decoupling coefficients and Q factors, along with the noise correlation matrix, are shown in Fig. 2.

Experimental methods

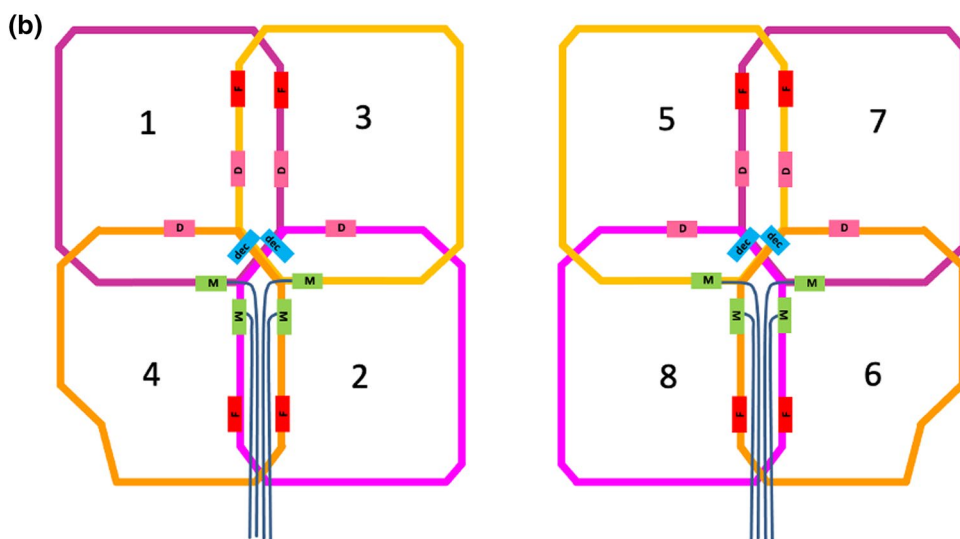
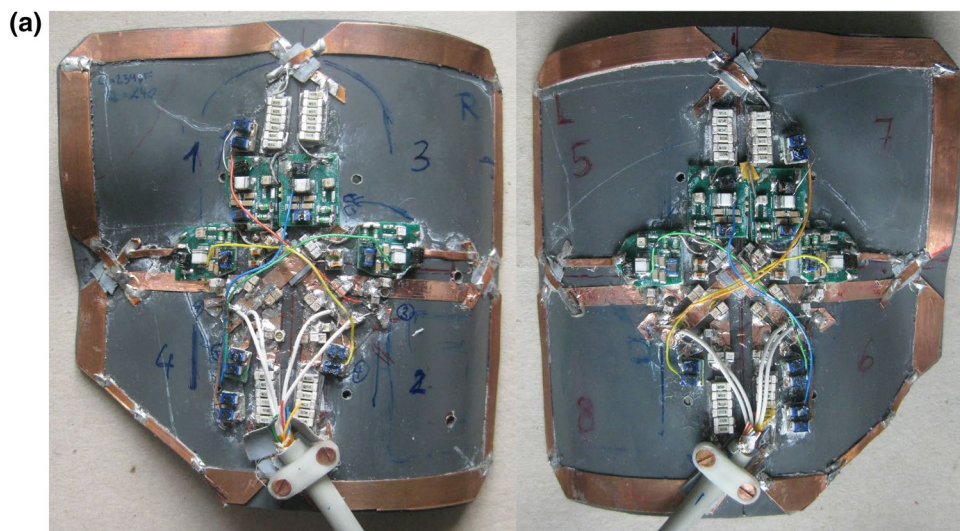
Experiments were performed using a contemporary whole body 0.55 T system (prototype MAGNETOM Aera, Siemens Healthineers, Erlangen, Germany) equipped with high-performance shielded gradients (45 mT/m amplitude, 200 T/m/s slew rate) [21]. RF transmission was performed with the integrated body coil, and signal reception was performed with the integrated body coil or with a dedicated 8-channel UA coil or the 16-channel HN coil, both shown in Fig. 3. Note that in the UA coil, there is plastic holder that allows the arrays to be adjusted and fixed to the patient's anatomy (Fig. 3, center). This allows the elements of the UA coil to be placed closer to the articulators than those of the HN coil.

Volumetric data of the upper airway were acquired using a 3D spoiled gradient echo sequence. Imaging parameters were: flip angle = 10° , TE = 5 ms, TR = 10 ms, FOV = $32 \times 32 \times 16 \text{ cm}^3$, resolution = $2.5 \times 2.5 \times 5 \text{ mm}^3$, receiver bandwidth = 150 Hz/pixel, and k_y and k_z phase encodings along A–P and R–L directions, respectively. Four subjects were scanned in a supine position under a protocol approved by our Institutional Review Board. Figure 4 illustrates the eleven VOIs used for SNR evaluation. The VOIs are: 1. Upper lip, 2. Lower lip, 3. Anterior tongue, 4. Middle tongue, 5. Posterior tongue, 6. Velum, 7. Pharyngeal wall, 8. Pons, 9. Frontal lobe, 10. Cerebellum, 11. Occipital lobe. The VOIs were chosen as they comprise the majority of the main articulators. Each VOI was generated using the 3D manual segmentation tools of ITK-SNAP (www.itk-snap.org) [22].

Signal-to-noise ratio (SNR)

Pre-scan noise used for noise pre-whitening was acquired with 256×128 samples per channel. Images were reconstructed using IFFT and coils sensitivity maps were

Fig. 1 Design and layout of the custom upper airway (UA) coil. **a.** Both phased arrays were attached to an anatomically shaped PVC cover. Electronics for matching, decoupling, and detuning were then added. Note the coil overlap to minimize decoupling. **b.** Schematic of the phased arrays. Each element contains a decoupling network (D), matching network (M), and an RF fuse (F) for subject safety during RF transmission. In addition, the diagonal elements share a common rung with a capacitor for capacitive decoupling (dec)



estimated from 26 central k-space lines. Image and coil sensitivity data were pre-whitened prior to SNR evaluation. SNR maps were computed following Roemer's formulation for phased array combined image reconstruction [23]:

$$SNR = \frac{\sqrt{2} |b^H p|}{\sqrt{(b^H b)}}, \quad (1)$$

where \mathbf{p} is the vector of complex image values for each coil, and \mathbf{b} is the vector of complex coil sensitivities. Using this formulation using pre-whitened data along with proper scaling of the signal to preserve the same effective gain as the noise leads to pixel intensities in SNR units [24].

To compare the SNR efficiency of both coils (UA and HN coils), each coil was first compared to the integrated body coil by performing the imaging sequence without patient repositioning. This allowed per-pixel calculation of SNR

gains for each of UA and HN coils relative to the body coil. The ratio of SNR gains for each coil ($rSNR$) was obtained as follows: $rSNR_{UA} = SNR_{UA}/SNR_{body}$ and $rSNR_{HN} = SNR_{HN}/SNR_{body}$. Subsequently, the ratio of the relative SNR ($rSNR_{UA}/rSNR_{HN}$) was obtained in each VOI to directly compare the performance of the UA coil with the HN coil.

Parallel imaging performance

G-factor maps were calculated for both, conjugate gradient (CG) SENSE with uniform density undersampling (UD), and with a variable density (VD) Cartesian trajectory using 32 fully-sampled central lines. We synthesized 2D data by performing an IFFT of the 3D data in the slice-encoding direction and retrospectively undersampled this fully sampled 2D data that was acquired using the 8-channel UA coil from subject 1. We tested acceleration factors (R) of 2, 3, and 4.

Element Size	79 × 74 mm
Conductor Thickness	200 μm
Geometric Decoupling Coefficient	> -22 dB
Capacitive Decoupling Coefficient	> -25 dB
Typical Q-unloaded	228
Typical Q-loaded	135
Typical Q-ratio	1.7

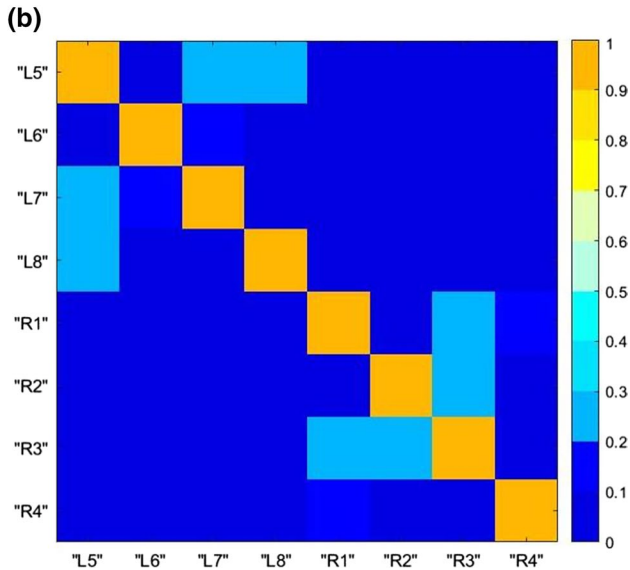


Fig. 2 Physical and noise characteristics of the upper airway coil. **a.** Element dimensions, decoupling coefficients, and Q factors. **b.** Noise correlation matrix of all eight channels. R = right, L = left

For arbitrary sampling trajectories, the image \mathbf{v} can be reconstructed from pre-whitened data by solving $(E^H E)\mathbf{v} = E^H \mathbf{m}$, where E is the encoding matrix and \mathbf{m} is the sampled pre-whitened k-space data [25]. The previous equation can be iteratively solved using conjugate gradients (CG) to approximate the image as $\mathbf{v} = (E^H E)^{-1} E^H \mathbf{m}$. In this case, the g-factor at pixel ρ is defined as [26]:

$$g_\rho = \sqrt{[(E^H E)^{-1}]_{\rho,\rho} (E^H E)_{\rho,\rho}} \quad (2)$$

Results

The SNR gains over the body coil for both, the UA coil and the HN coil, can be seen in Fig. 5.

The posture was slightly different for these two scans and are spatially co-registered for display. Notice that the UA coil generally has a higher relative SNR in the upper airway regions of interest such as the lips, tongues, velum, and pharyngeal wall, and the HN coil generally has higher relative SNR in the brain, as expected.

The ratio of relative SNR ($rSNR_{UA} / rSNR_{HN}$) quantifies the performance of the UA coil relative to that of the HN coil. Figure 6 shows the resulting relative ratio over all the VOIs. Significant SNR improvement is observed in all upper airway VOIs in all subjects. The gain was strongest in the upper and lower lip areas for all subjects, with approximately fourfold improvement for subject 1 and was as low as 3 for subject 4. This inter-subject variation in the upper airway is likely due to head size and variations in placement of the left and right-side UA coil arrays (see Fig. 3). The HN coil outperformed the UA coil in regions closer to the brain, such as the frontal lobe.

We evaluated the parallel imaging performance of both coils. Figure 7 contains g-factor maps, along with reconstructed images with 15 iterations. For the UA coil with $R=2$ and 3, both UD and VD trajectories have g-factor values below 1.1 in the upper airway region, allowing for sufficient image quality. For $R=4$, the g-factor values are higher for both trajectories, resulting in a noisier reconstruction. For the HN coil with $R=2$, both the UD and VD g-factors are below 1.1 which results in low noise amplification. For $R=3$, the g-factors are below 1.3, which can result in more



Fig. 3 Custom upper airway (UA) and prototype head-neck (HN) coil for 0.55 Tesla MRI. (Left) 8-channel UA coil before adjustment of coil elements. (Center) UA coil with coil elements placed as close as possible to the upper airway region without contacting the skin or otherwise altering speech production. A 9th element can be placed in

between the elements for increased SNR, if the subject's head size allows. (Right) 16-channel HN coil. The UA coil can be placed closer to the vocal tract articulators of interest and excludes signal and noise from the brain

Fig. 4 Upper airway volumes-of-interest (VOIs). Intersection of the VOIs with a mid-sagittal slice acquired using the (left) UA coil and (right) HN coil

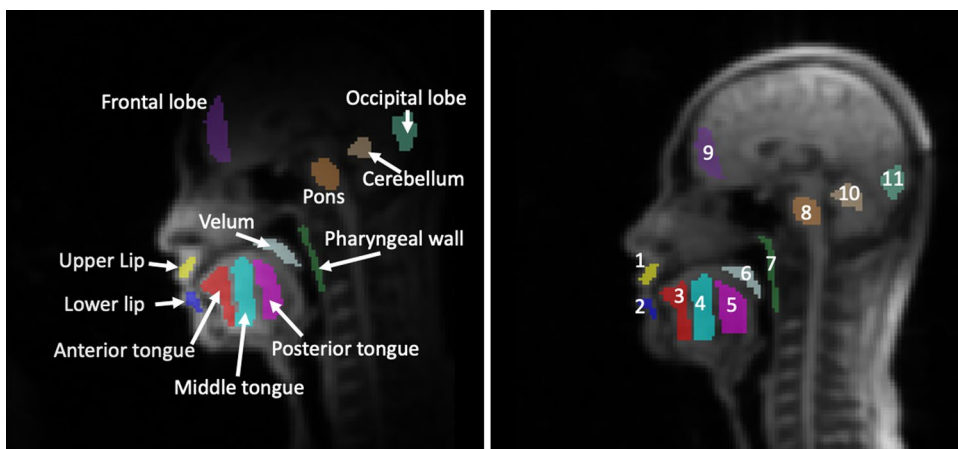


Fig. 5 Relative SNR ($rSNR = SNR_{coil} / SNR_{body}$). In all four subjects, the UA coil provided a significant SNR gain in the upper airway VOIs (white arrows). The HN coil provided significantly higher SNR in the brain (red arrow), as expected

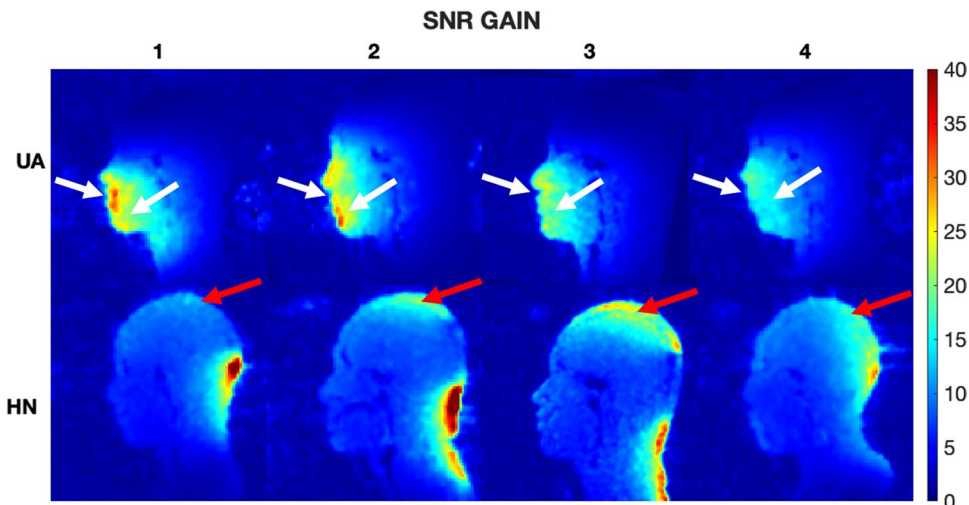
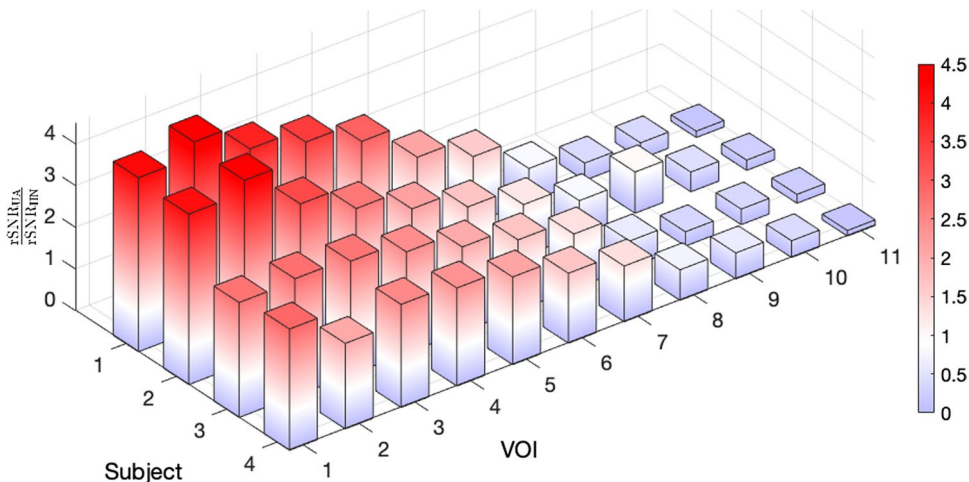


Fig. 6 Relative SNR of the UA coil compared to the HN coil ($rSNR_{UA} / rSNR_{HN}$). The height and color of the bars represent relative SNR. The UA coil outperforms the HN coil in vocal tract VOIs (VOIs 1–7). VOIs with a reddish hue exhibit a ratio greater than 1 (UA outperforms HN), whereas VOIs with a bluish hue exhibit a ratio less than 1 (HN outperforms UA). The biggest improvement is in the upper and lower lip with 4.3-fold relative SNR



noise amplification. For $R=4$, the g-factors are higher and the reconstruction is too noise to be of use. Overall, the UA coil g-factor maps are lower than those of the HN coil for all accelerations, resulting from the higher sensitivity difference in the sagittal plane of the UA coil elements.

Discussion

In this study, we demonstrated a dedicated UA coil that exhibited a significant increase in SNR over the HN coil in

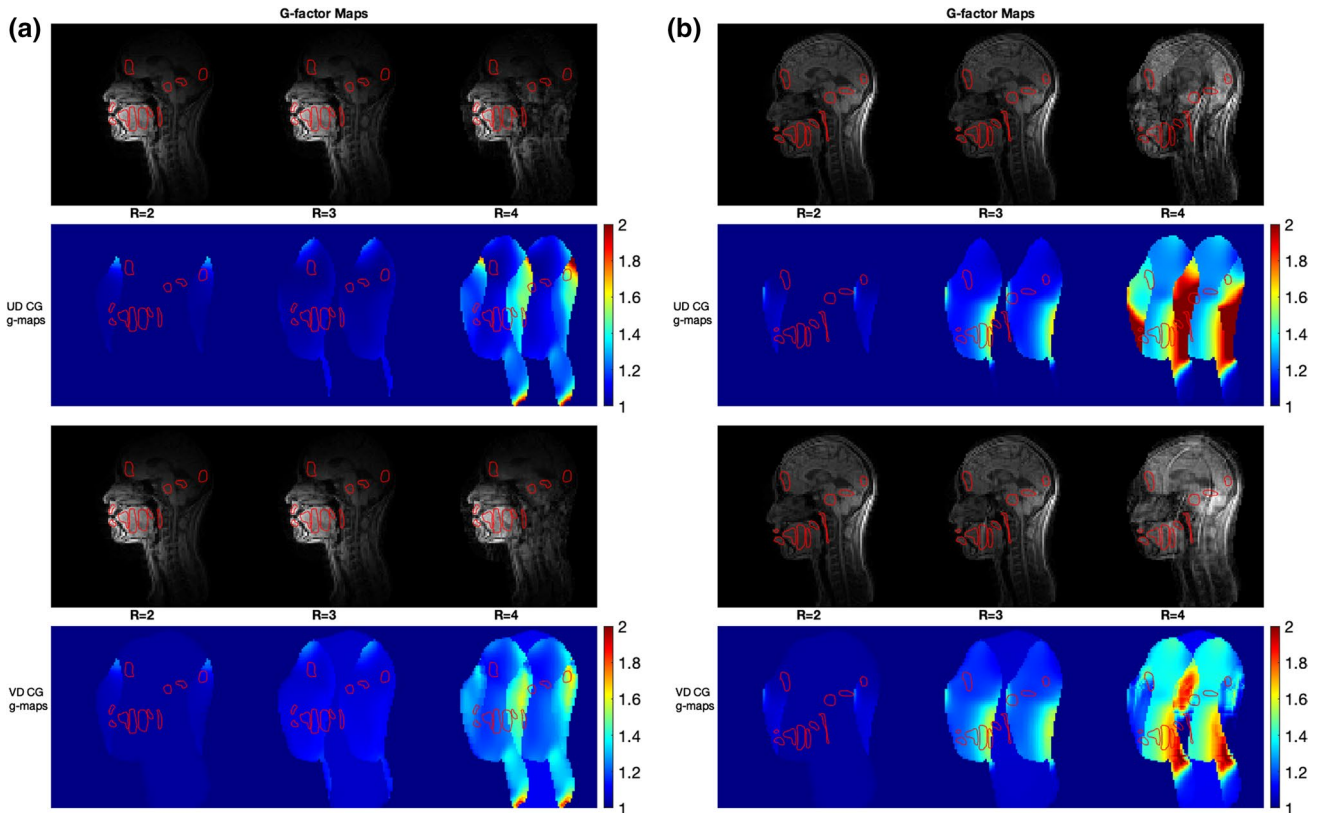


Fig. 7 Parallel imaging performance for 2D MRI of a mid-sagittal slice with anterior–posterior undersampling and acceleration factor of 2, 3, and 4. Results are shown for the **a.** UA coil and **b.** HN coil. For both figures, the first and third rows show UD CG and VD CG reconstructions, respectively, and the second and fourth rows show UD CG and VD CG g-maps, respectively. Results from one representative subject are shown. For the UA coil with R=2 and 3, g values average

about 1.1 in the upper airway region for both trajectories, allowing for good image quality for speech imaging. At R=4, g values are higher (about 1.6), resulting in a noisier reconstruction. For the HN coil, R=2 and 3 g factors still allow for good image quality, but at R=4 the image is again too noisy to be of use. Note that the g factors of the UA coil are lower than that of the HN coil for all accelerations

upper airway regions of interest that are relevant to speech production. The highest observed SNR gain was three- to fourfold in the upper and lower lip region.

The placement of UA coil elements close to the cheeks allows for a high SNR gain near the articulators, while the gain is negligible near the pharyngeal wall, which is the deepest boundary of interest. The high SNR near the articulators is beneficial for upper airway imaging, as it mitigates g-factor noise amplification allowing for better image quality [27].

The thermal noise standard deviation in MRI is given by the classic relation $\sqrt{4kT\Delta fR}$, where k is the Boltzmann constant, T the temperature in K, and Δf the receiver bandwidth. If the coil is unloaded, the resistance R is the resistance of the coil R_{coil} , while for loaded conditions, the total resistance R is $R_{coil} + R_{sample}$, where R_{sample} is the resistance of the sample which characterizes the induced eddy current losses in the conductive sample [28]. We denote the quantity $SNR_{intrinsic}$ as the SNR that would be achieved with a lossless coil (e.g., super-conducting lossless coil), and $SNR_{obtained}$, as

the SNR that is obtained considering coil losses. From the noise standard deviation expression above, we see that SNR is proportional to $\frac{1}{\sqrt{R}}$. We then obtain:

$$\frac{SNR_{obtained}}{SNR_{intrinsic}} = \sqrt{\frac{R_{sample}}{R_{sample} + R_{coil}}}. \quad (3)$$

The quality factor of a coil can be expressed as $Q = \frac{\omega L}{R}$. Where ω is the operating angular frequency, R is the total resistance, and L is the coil's inductance [29]. Denoting Q_u and Q_l as the unloaded and loaded quality factors, we can define their ratio $Q_{ratio} = \frac{Q_u}{Q_l}$. We can then express (Eq. 3) as:

$$SNR_{obtained} = SNR_{intrinsic} \sqrt{1 - \frac{1}{Q_{ratio}}}. \quad (4)$$

Equation 4 allows us to express the obtained SNR as a fraction of the intrinsic SNR using the Q_{ratio} . A higher effective sample resistance results in larger coil loading, which increases the Q_{ratio} , and thus the obtained SNR is a larger

fraction of the intrinsic SNR. The resistance of a spherical sample is related to the frequency and the sample size as $R_{sample} \propto \omega^2 d^5$, where d is the radius of the sample [30]. The coil resistance is dominated by the skin effect: $R_{coil} \propto \sqrt{\omega}$ [31].

From the above equations, we see that at higher fields, the resistance of the sample dominates, and thus coil losses contribute less to the overall SNR. Typical values of unloaded and loaded Q factors at 1.5 T are 350 and 50, respectively [29]. Using Eq. 4 with these typical Q factor values, we see that the obtained SNR is 93% of the intrinsic SNR, meaning that if an ideal lossless coil was used, the SNR improvement would be only about 7%. This improvement diminishes for larger fields. Due to the above-mentioned frequency dependencies of coil and sample resistances, it can be seen that at lower fields the coil resistance is comparable to that of the sample, thus coil losses become more important. To address this, the UA coil aimed to increase the Q_{ratio} utilizing thick copper bands to decrease the coil resistance and was placed closer to the subject to increase loading. This resulted in a Q ratio of about 1.7 (see Fig. 2a), which means that the obtained SNR is about 65% of the intrinsic SNR. This is a well-accepted value, as it is very difficult to get better performance without using super-conducting low-loss coils.

There is also an opportunity to develop denser arrays with smaller elements. However, minimizing coil size amplifies the contribution of coil losses. In the present coil, the element size is designed for deeper structures. For even faster imaging, a design with more elements may help acceleration (if g-factors allow for this). This could provide even higher SNR near the surface. With a tradeoff for loading factor at this low frequency, the contribution of coil losses will increase significantly and SNR at depth will decrease. Inductive coupling between elements at low frequency will also increase noise, and this effect can be worse for more elements.

Conclusion

The novel UA coil showed a 1.3 to 4.6-fold improvement in SNR over the HN coil in VOIs that are relevant to speech production. The g-factor values for the UA coil in the upper airway regions were below 1.1 for $R=2$ and 3, for uniform and variable density Cartesian undersampling schemes with CG SENSE reconstruction. This is favorable for high-performance speech production dynamic MRI at 0.55 Tesla.

Supplementary Information The online version contains supplementary material available at <https://doi.org/10.1007/s10334-022-01036-0>.

Acknowledgements We acknowledge grant support from the National Science Foundation (#1828736) and research support from Siemens Healthineers.

Data availability statement Data and code from this work are available at: Code: github.com/usc-mrel/speech_coil_eval, Data: zenodo.org/record/5898595.

Declarations

Conflict of interest Dr. Sophia Cui is an employee of Siemens Healthcare.

Ethical standards All procedures involving human subjects were in accordance with the local ethics board.

Informed consent Written informed consent was obtained in all cases.

References

- Bresch E, Yoon-Chul K, Nayak K et al (2008) Seeing speech: capturing vocal tract shaping using real-time magnetic resonance imaging [Exploratory DSP]. *IEEE Signal Process Magn* 25:123–132. <https://doi.org/10.1109/MSP.2008.918034>
- Scott AD, Wylezinska M, Birch MJ, Miquel ME (2014) Speech MRI: Morphology and function. *Physica Med* 30:604–618. <https://doi.org/10.1016/j.ejmp.2014.05.001>
- Pauloski BR, Logemann JA, Rademaker AW et al (1993) Speech and swallowing function after anterior tongue and floor of mouth resection with distal flap reconstruction. *J Speech Lang Hear Res* 36:267–276. <https://doi.org/10.1044/jshr.3602.267>
- Wyatt R, Sell D, Russell J et al (1996) Cleft palate speech dissected: a review of current knowledge and analysis. *Br J Plast Surg* 49:143–149. [https://doi.org/10.1016/S0007-1226\(96\)90216-7](https://doi.org/10.1016/S0007-1226(96)90216-7)
- Cao B, Sebkhi N, Mau T et al (2019) Permanent Magnetic Articulograph (PMA) vs Electromagnetic Articulograph (EMA) in Articulation-to-Speech Synthesis for Silent Speech Interface. In: *Proceedings of the eighth workshop on speech and language processing for assistive technologies*. Association for computational linguistics, Minneapolis, Minnesota, pp 17–23
- Rebernik T, Jacobi J, Jonkers R et al (2021) A review of data collection practices using electromagnetic articulography. *Lab Phonol: J Assoc Lab Phonol* 12:6. <https://doi.org/10.5334/labphon.237>
- Preston JL, Leece MC, Maas E (2016) Intensive treatment with ultrasound visual feedback for speech sound errors in childhood Apraxia. *Front Hum Neurosci*. <https://doi.org/10.3389/fnhum.2016.00440>
- Weis S, Logemann JA, Colangelo L (2000) Effects of three techniques on maximum posterior movement of the tongue base. *Dysphagia* 15:142–145. <https://doi.org/10.1007/s004550010016>
- Hayes A, Alspaugh JM, Bartelt D et al (2009) Radiation safety for the speech-language pathologist. *Dysphagia* 24:274–279. <https://doi.org/10.1007/s00455-008-9201-0>
- Schenck JF (1996) The role of magnetic susceptibility in magnetic resonance imaging: MRI magnetic compatibility of the first and second kinds. *Med Phys* 23:815–850. <https://doi.org/10.1118/1.597854>
- Lim Y, Lingala SG, Narayanan SS, Nayak KS (2019) Dynamic off-resonance correction for spiral real-time MRI of speech. *Magn Reson Med* 81:234–246. <https://doi.org/10.1002/mrm.27373>
- Lim Y, Bliesener Y, Narayanan S, Nayak KS (2020) Deblurring for spiral real-time MRI using convolutional neural networks. *Magn Reson Med* 84:3438–3452. <https://doi.org/10.1002/mrm.28393>

13. Lim Y, Nayak KS (2022) Real-time MRI of speech production at 0.55 Tesla. In: ISMRM 31st Scientific Session. London, England, United Kingdom
14. Bhattacharya I, Ramasawmy R, Restivo MC, Campbell-Washburn AE (2019) Dynamic speech imaging at 0.55T using single shot spirals for 11ms temporal resolution. In: ISMRM 27th Scientific Session. Montreal QC, Canada
15. Symms M (2004) A review of structural magnetic resonance neuroimaging. *J Neurol Neurosurg Psychiatry* 75:1235–1244. <https://doi.org/10.1136/jnnp.2003.032714>
16. Plantinga BR, Temel Y, Roebroek A et al (2014) Ultra-high field magnetic resonance imaging of the basal ganglia and related structures. *Front Hum Neurosci* 8
17. Nayak KS, Lim Y, Campbell-Washburn AE, Steeden J (2022) Real-time magnetic resonance imaging. *J Magn Reson Imaging* 55:81–99. <https://doi.org/10.1002/jmri.27411>
18. Kim Y-C, Hayes CE, Narayanan SS, Nayak KS (2011) Novel 16-channel receive coil array for accelerated upper airway MRI at 3 Tesla. *Magn Reson Med*. <https://doi.org/10.1002/mrm.22742>
19. Lingala SG, Zhu Y, Kim Y et al (2017) A fast and flexible MRI system for the study of dynamic vocal tract shaping. *Magn Reson Med*. <https://doi.org/10.1002/mrm.26090>
20. Hon Tat Hui (2008) Decoupling methods for the mutual coupling effect in antenna arrays: a review. *Recent Patents Eng* 1:187–193. <https://doi.org/10.2174/187221207780832200>
21. Campbell-Washburn AE, Ramasawmy R, Restivo MC et al (2019) Opportunities in interventional and diagnostic imaging by using high-performance low-field-strength MRI. *Radiology* 293:384–393. <https://doi.org/10.1148/radiol.2019190452>
22. Yushkevich PA, Piven J, Hazlett HC et al (2006) User-guided 3D active contour segmentation of anatomical structures: significantly improved efficiency and reliability. *Neuroimage* 31:1116–1128. <https://doi.org/10.1016/j.neuroimage.2006.01.015>
23. Roemer PB, Edelstein WA, Hayes CE et al (1990) The NMR phased array. *Magn Reson Med* 16:192–225. <https://doi.org/10.1002/mrm.1910160203>
24. Kellman P, McVeigh ER (2005) Image reconstruction in SNR units: a general method for SNR measurement. *Magn Reson Med* 54:1439–1447. <https://doi.org/10.1002/mrm.20713>
25. Pruessmann KP, Weiger M, Bö P, Boesiger P (2001) Advances in Sensitivity Encoding With Arbitrary k-Space Trajectories
26. Akcakaya M, Basha TA, Manning WJ, Nezafat R (2014) Efficient calculation of g-factors for CG-SENSE in high dimensions: noise amplification in random undersampling. *J Cardiovasc Magn Reson* 16:W28. <https://doi.org/10.1186/1532-429x-16-s1-w28>
27. De Zwart JA, Ledden PJ, Van Gelderen P et al (2004) Signal-to-noise ratio and parallel imaging performance of a 16-channel receive-only brain coil array at 3.0 tesla. *Magn Reson Med* 51:22–26. <https://doi.org/10.1002/mrm.10678>
28. Fujita H, Zheng T, Yang X et al (2013) RF surface receive array coils: the art of an LC circuit: RF surface receive array coils. *J Magn Reson Imaging* 38:12–25. <https://doi.org/10.1002/jmri.24159>
29. Corea JR, Lechene PB, Lustig M, Arias AC (2017) Materials and methods for higher performance screen-printed flexible MRI receive coils: high-performance screen-printed flexible MRI receive coils. *Magn Reson Med* 78:775–783. <https://doi.org/10.1002/mrm.26399>
30. Hoult DI (1969) Lauterbur PC (1979) The sensitivity of the zeugmatographic experiment involving human samples. *J Magn Reson* 34:425–433. [https://doi.org/10.1016/0022-2364\(79\)90019-2](https://doi.org/10.1016/0022-2364(79)90019-2)
31. Giovannetti G, Hartwig V, Landini L, Santarelli MF (2012) Classical and lateral skin effect contributions estimation in strip MR coils. *Concepts Magn Reson* 41B:57–61. <https://doi.org/10.1002/cmr.b.21210>

Publisher's Note Springer Nature remains neutral with regard to jurisdictional claims in published maps and institutional affiliations.

Springer Nature or its licensor holds exclusive rights to this article under a publishing agreement with the author(s) or other rightsholder(s); author self-archiving of the accepted manuscript version of this article is solely governed by the terms of such publishing agreement and applicable law.